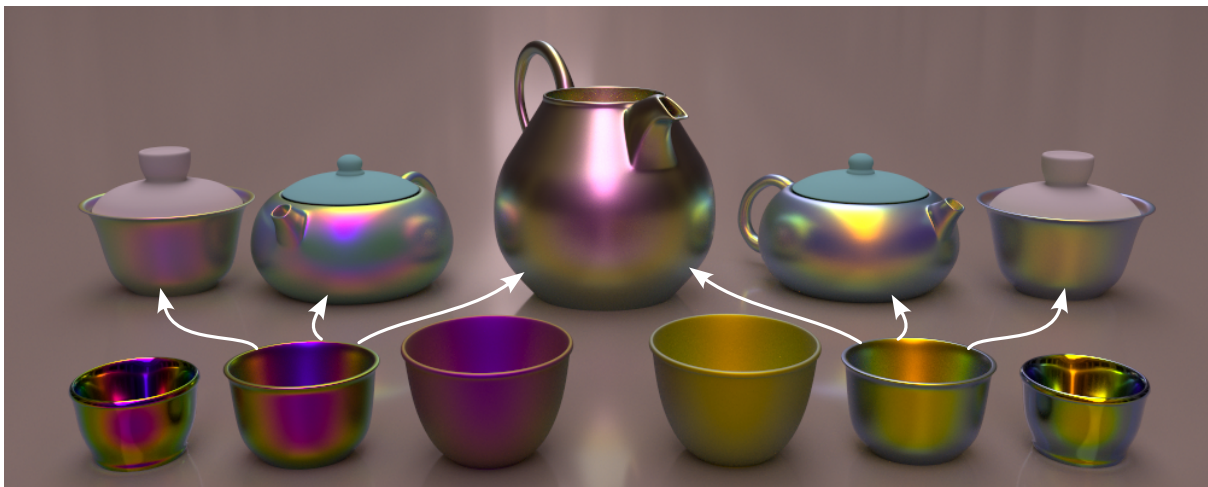# Interactive Exploration of Vivid Material Iridescence using Bragg Mirrors

G. Fourneau, R. Pacanowski, P. Barla

INRIA, Univ. Bordeaux, CNRS, Bordeaux INP, LaBRI, UMR 5800, France

FIGURE 1 – *Layered Bragg structures exhibit a wide range of iridescent colors. Bottom row : we show two different types of Bragg mirrors (left : $n_2 = 1.5$, $d_1 = 125nm$, $d_2 = 375nm$, right : $n_2 = 1.5$, $d_1 = 101nm$, $d_2 = 143nm$ — $n_1 = 1$ and $N = 20$ in both cases), with increasing roughness toward the center of the image ($\alpha \in \{0.025, 0.1, 0.4\}$). Top row : we combine the two Bragg layers with $\alpha = 0.1$ (left one on right one) on the teapot at the center, and each layer individually on a pair of Lambertian materials (see lids) : one achromatic, the other colored.*

Abstract

Many animals, plants or gems exhibit iridescent material appearance in nature. These are due to specific geometric structures at scales comparable to visible wavelengths, yielding so-called structural colors. The most vivid examples are due to photonic crystals, where a same structure is repeated in one, two or three dimensions, augmenting the magnitude and complexity of interference effects. In this paper, we study the appearance of 1D photonic crystals (repetitive pairs of thin films), also called Bragg mirrors. Previous work has considered the effect of multiple thin films using the classical transfer matrix approach, which increases in complexity when the number of repetitions increases. Our first contribution is to introduce a more efficient closed-form reflectance formula [Yeh88] for Bragg mirror reflectance to the Graphics community, as well as an approximation that lends itself to efficient spectral integration for RGB rendering. We then explore the appearance of stacks made of rough Bragg layers. Here our contribution is to show that they may lead to a ballistic transmission, significantly speeding up position-free rendering and leading to an efficient single-reflection BRDF model.

CCS Concepts

• *Computing methodologies* → *Reflectance modeling;*

1. Introduction

Iridescence, or goniochromism, is a fascinating phenomenon that can be observed in nature in a variety of materials, such as peacock feathers, butterfly wings of beetle shells (see Stavenga [Sta14] for an overview). This property refers to a material's ability to change color when viewed from different angles. Iridescence is the result of structural colors, where the interaction of light waves with fine structures generates colors by interference.

There are several types of structures that can produce iridescence. Thin films, diffraction gratings, and photonic crystals are among them. The latter are periodic *dielectric* structures, where repetitions may occur in one, two or three dimensions. In this paper, we focus on 1D photonic crystals, also known as Bragg mirrors, which use periodic repetitions of thin layers with two different optical indices. They are found in a variety of biological structures, notably in beetles as shown in Figure 2(a-c). However, rendering materials based on Bragg mirrors is challenging, as they produce complex spectra, both in reflection and transmission. Our goal is to introduce rendering techniques that grant interactive exploration of materials based on Bragg mirrors.

A first difficulty lies in the reflectance spectra of Bragg mirrors : with an increasing number of periodic repetitions, high-frequency spectral oscillations start to appear, except for subsets of wavelengths called *photonic band gaps* where reflectances reach values close to one (see Figure 3), which is the main cause for the observed vivid reflectance colors. Our first contribution (Section 3) is to simplify reflectance evaluation. Our approach relies on the closed-form spectral reflectance formula of Pochi Yeh [Yeh88], which to the best of our knowledge has never been introduced to the Computer Graphics community. Compared to the standard transfer matrix approach, it has the advantage of being independent of the number of periodic repetitions. Besides performance, it provides insights on the structure of a Bragg mirror reflectance spectrum, notably the location of its band gaps. We use these insights to derive an approximate Bragg reflectance spectrum that lends itself to a fast, closed-form spectral integration for RGB rendering. This is particularly useful to quickly explore the effect of different combinations of Bragg mirror parameters on iridescent material appearance.

A second difficulty is due to the spatial configuration of Bragg mirrors. Taking inspiration from biological structures, we consider materials made of one or more layers of Bragg mirrors distributed in various orientations, on top of a diffuse opaque base (see Figure 2(d,e)). Bragg layers are modelled using microfacet theory, where each microfacet is a tiny Bragg mirror. Since only dielectric media are involved, a significant proportion of the incoming light reaching a Bragg layer is transmitted to layers below. Our second contribution (Section 4) is to show that if the refractive index is the same on both sides, the spectral transmission of a Bragg layer is ballistic and can thus be efficiently pre-integrated over Bragg mirror orientations, significantly simplifying the rendering of the layer stack. We then use this property to derive a single-reflection model that further speeds up the rendering process, granting interactive feedback in spectral renderings.

We finally explore the expressivity of layered Bragg structures (Section 5) through several parameter variations (e.g., see Figure 1). Our experiments show that the appearance of materials based on Bragg mirrors differ qualitatively from other 1D iridescent structures, such as those based on thin-films or pearlescent flakes. We validate our model by comparing rendered and measured scatterograms, demonstrating qualitatively similar results.

2. Previous work

Some of the most striking examples of iridescence occur in nature. An archetypal example is the Morpho butterfly, whose scales have been extensively studied in both the Optics (e.g., [OZC*13]) and Computer Graphics (e.g., [Sun06, MMRO13, kWwZ15]) communities. Iridescent structures may also be artificially manufactured, their complexity ranging from diffraction gratings (e.g., [Sta99, SFDC00]), to surfaces with nano-particles deposited on one or multiple thin-films (e.g, [YLL*18, VPA*22]) or self-assembled cholesteric structures (e.g., [GAVH16]).

In this paper, we focus on one-dimensional structures, whereby interference is due to the stacking of multiple thin films. Since the pioneering work of Smits and Meyer [SM92] in Computer Graphics, a number of methods dedicated to the rendering of iridescent appearance due to thin-films have been introduced.

Single thin-film. In the context of Monte-Carlo path-tracing, Gondek [GMN94] was one of the first to simulate interferences due to a single thin film. Sun et al. [SW08] derived a closed-form formulae for the reflectance of a thin-film coated over a transparent or opaque layer. Belcour and Barla [BB17] introduced a fast RGB model that predicts accurately the colors of a thin-film for a microfacet BRDF. Their work was improved by Keniphof et al. [KGK19, KK22] for the real-time rendering of rough iridescent surfaces, and by Guo et al. [GCGP18] for special effect pigments.

Multiple thin-films. Icart et Arques [IA00] introduced a BRDF model based on the formalism of Abeles matrices (similar to transfer matrices) for multiple thin-films. They demonstrate results for up to 4 repetitions of two layers on top of a conductor. Since our model does not rely on transfer matrices, it remains computationally efficient regardless of the number of repetitions of the physical structure. Hirayama et al. [HKYM01] introduced a model with a recursive formulation that approximates the appearance of multiple thin-films but is only valid for smooth materials. The approach of Imura et al. [IOS*09] unifies the treatment of gratings and multi thin-films for real-time rendering at the expense of precomputation. Sun et al. [Sun06] takes into account multiple thin-film coatings with less precomputation thanks to a closed-form solution. However, they must assume that a layer of air is present between each thin film. We consider similar structures called Bragg mirrors, which consist of several repetitions of pairs of thin-films.

Pearlescent materials Iridescent effects are also found in special effect paints that incorporate pearlescent flakes. Most previous work in Computer Graphics (e.g., [EKM01, SMAS08, EÖÖ16, BP20]) relies on transfer matrices to compute the reflectance of such flakes. The general framework introduced by Guillen et al. [GMG*20] handles iridescent flakes embedded in a dielectric resin. It grants control over the distribution of flake orientations, as well as their density, among other parameters. Like pearlescent materials, layered Bragg structures may produce a wide range of iridescent color fringes. However, they differ in their nature : Bragg mirrors only consist of dielectric media and are organized in layers, whereas pearlescent flakes always involve conductors and are distributed in a volume. As a result, their appearance is qualitatively different, as further discussed in Section 5.

3. Bragg mirrors

We consider iridescent materials where structural colors are due to interference in 1D photonic crystals, also called Bragg mirrors. We begin in Section 3.1 by recalling the steps that yield to Yeh's closed-form spectral reflectance formula. We then present in Section 3.2 an approximation of this spectrum that enables fast spectral integration for interactive RGB rendering.

3.1. Spectral reflectance

A Bragg mirror is a medium made of N identical cells, each cell a pair of media characterized by their indices n_1 and n_2 and their thicknesses d_1 and d_2, and separated by smooth interfaces, as shown in Figure 2(d). The refractive indices may be complex in general, but we will focus on the case of real indices in this work, as these are ubiquitous in biological and mineral iridescent materials. We write $\Lambda = d_1 + d_2$ the thickness of a cell. When Λ is comparable to visible light wavelengths (a few hundreds of nanometers), this leads to interference effects that produce vivid iridescent colors. We only describe the reflectance R_λ of a Bragg mirror since with real indices its transmittance is given by $T_\lambda = 1 - R_\lambda$. Perpendicular ('s') and parallel ('p') polarizations are considered independently.

In order to understand the interference effects that occur in a Bragg mirror, one must relate electro-magnetic fields on either sides of the structure. The electromagnetic field in each medium may be written as the sum of two fields : one propagating downward, and the other upward, with respective amplitudes a and b, as illustrated in Figure 2(d). The transfer matrix formalism is then classically used to relate the fields in neighboring media ; we refer the reader to the work of Yeh [Yeh88] for a didactic introduction to this formalism. An important property of Bragg mirrors is that their structure is periodic ; hence we only need to characterize the transfer matrix from one cell to another – called a *translation* matrix. With a Bragg mirror made of N cells, this leads to :

$$\begin{pmatrix} a_0 \\ b_0 \end{pmatrix} = \begin{bmatrix} A & B \\ C & D \end{bmatrix}^N \begin{pmatrix} a_N \\ b_N \end{pmatrix}, \tag{1}$$

where A, B, C and D characterize the translation matrix, while a_0 and b_0 are the incident and reflected field amplitudes respectively, a_N is the transmitted field amplitude, and $b_N = 0$ in our case (no upward propagating field from below when considering reflectance).

The coefficient of reflection of a Bragg mirror is defined as $r_N = b_0/a_0$, where a_0 and b_0 are computed using Equation 1. Yeh gives a direct analytical formulation of the reflectance $R_\lambda = |r_N|^2$ that does not require the multiplication of N translation matrices :

$$R_\lambda = \frac{|C|^2}{|C|^2 + \left(\frac{\sin K\Lambda}{\sin NK\Lambda} \right)^2}, \tag{2}$$

where C comes from the translation matrix, and K is the so-called Bloch wavenumber, which characterizes the propagation of a wave in a periodic medium. It is given by the dispersion relation :

$$cos(K\Lambda) = \frac{A+D}{2}, \tag{3}$$

where A and D are coefficients of the translation matrix given by

$$A = e^{ik_{1z}d_1} \left(\cos k_{2z}d_2 + \tfrac{1}{2} i\Omega \sin k_{2z}d_2 \right), \tag{4}$$

$$D = e^{-ik_{1z}d_1} \left(\cos k_{2z}d_2 - \tfrac{1}{2} i\Omega \sin k_{2z}d_2 \right), \tag{5}$$

with $k_{iz} = \frac{2\pi n_i}{\lambda} \cos\theta_i$ the wavevector in the medium $i \in \{1,2\}$ projected on the z direction (normal to the structure), θ_i the ray angle in medium i, and Ω a term that differs depending on polarization :

$$\Omega_s = \frac{k_{2z}}{k_{1z}} + \frac{k_{1z}}{k_{2z}} = \frac{n_2 \cos\theta_2}{n_1 \cos\theta_1} + \frac{n_1 \cos\theta_1}{n_2 \cos\theta_2}; \tag{6}$$

$$\Omega_p = \frac{n_1^2 k_{2z}}{n_2^2 k_{1z}} + \frac{n_2^2 k_{1z}}{n_1^2 k_{2z}} = \frac{n_1 \cos\theta_2}{n_2 \cos\theta_1} + \frac{n_2 \cos\theta_1}{n_1 \cos\theta_2}. \tag{7}$$

Using Equations 4 and 5 in Equation 3, we obtain :

$$\cos(K\Lambda) = \cos k_{1z}d_1 \cos k_{2z}d_2 - \tfrac{1}{2}\Omega \sin k_{1z}d_1 \sin k_{2z}d_2. \tag{8}$$

Equation 8 may yield $|\cos(K\Lambda)| > 1$ in some configurations, leading to a complex-valued wavenumber. Such configurations are called *photonic band gaps* (BG), and are an important property of Bragg mirrors. Indeed, in these cases, waves propagating in the material are partially or totally forbidden to transmit through it due to destructive interferences, yielding a high reflectance as shown in Figure 3. Since band gaps depend on wavelength and angle of incidence, Bragg mirrors exhibit vivid iridescent colors.

In practice we must distinguish two cases : when K is real-valued, we may safely use Equation 2 ; whereas when K is complex-valued, we must instead use the following formula :

$$R_\lambda = \frac{|C|^2}{|C|^2 + \left(\frac{\sinh Im[K]\Lambda}{\sinh N Im[K]\Lambda} \right)^2}, \tag{9}$$

where $Im[K]\Lambda = -\ln(|\cos K\Lambda + \sin K\Lambda|)$. When N tends toward infinity, Equation 9 tends toward 1. The spectral reflectance R_λ of a Bragg mirror is thus highest in band gaps.

In both Equations 2 and 9, when $N = 1$ we have $|r_1|^2 = \frac{|C|^2}{|C|^2+1}$, yielding a direct formulation for $|C|^2 = \frac{|r_1|^2}{1-|r_1|^2}$. Here r_1 is the polarization-dependent reflection coefficient of a slab of index n_2 in a medium of index n_1, which is computed using Airy's summation :

$$r_1 = \frac{r_{12} + r_{21}e^{-2i\phi}}{1 + r_{12}r_{21}e^{-2i\phi}} = \frac{r_{12}(1 - e^{-2i\phi})}{1 - r_{12}^2 e^{-2i\phi}}, \tag{10}$$

with r_{ij} the Fresnel reflection coefficient at an interface between indices n_i and n_j with $r_{ij} = -r_{ji}$, and $\phi = \frac{2\pi}{\lambda} n_2 d_2 \cos\theta_2 = k_{2z}d_2$.

Figure 4 shows an exploration of the appearance of Bragg mirrors. Reflectance spectra, and thus colors, greatly vary with the angle of incidence. Compared to thin-films, Bragg mirrors exhibit much more vivid colors, especially around normal incidence.

3.2. RGB reflectance

Using Equations 2 and 9 inside and outside of band gaps respectively yields an efficient method for computing the spectral reflectance of a Bragg mirror, since increasing the number N of cells does
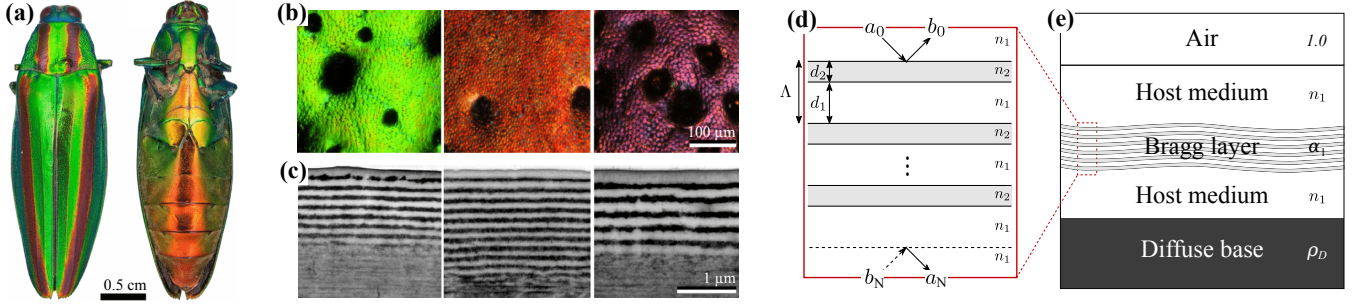
FIGURE 2 – *1D photonic crystals are commonly found in nature. Dorsal and ventral views (a) of a female Japanese jewel beetle, Chrysochroa fulgidissima. Microscopy (b) and TEM (c) images of its cuticle at different locations : the rough cuticle surface is shown in (b), while Bragg-like structures are observed in (c). All images from Schenck et al. [SWS13] –* © *IOP Publishing, reproduced with permission, all rights reserved. A Bragg mirror (d) is made of N cells, each composed of two thin films of different refractive indices (n_1, n_2) and thicknesses (d_1, d_2). The entry and exit refractive indices are equal, making the last interface index-matched (dashed line). A layered Bragg structure (e) consists of a rough Bragg layer (a contiguous distribution of Bragg mirrors of varying orientations) in a host medium of index n_1.*
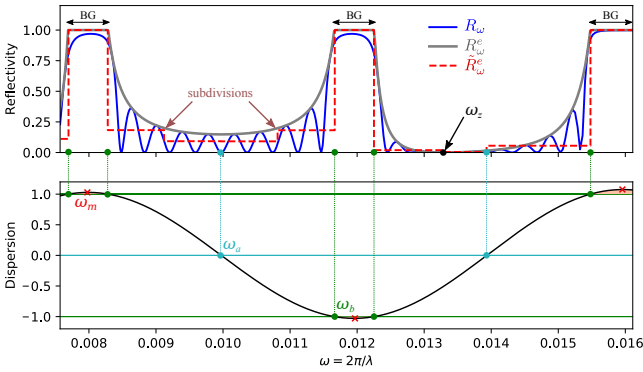
FIGURE 3 – *Top row : Reflectance spectrum R_ω (in blue) of a Bragg mirror, with $n_1 = 1$, $n_2 = 1.5$, $d_1 = d_2 = 315nm$ and $N = 10$. The reflectance envelope R_ω^e (in gray) equals 1 inside photonic band gaps (BG). Bottom row : the dispersion relation $\cos K\Lambda$ (in black) characterizes the location of a BG (it is either above 1 or below -1). Spectral modes ω_m (red crosses) always lie inside a BG and are used to find Airy points ω_a (in cyan) and BG edges ω_b (green dots). These spectral landmarks, along with zero points ω_z (in black) are used to define a piecewise-constant spectrum $\tilde{R}_\omega^e$ (dashed red curve in top row), which may be optionally subdivided.*

not increase computation complexity. Besides performance, the derivation of the previous section yields insights on the structure of the reflectance spectrum. We rely on these insights to provide a fast method for approximating the RGB reflectance of a Bragg mirror. The main idea is to use the dispersion relation to identify spectral landmarks (Section 3.2.1), from which a piecewise-constant approximation to Bragg mirror reflectance is derived (Section 3.2.2), granting a fast and accurate spectral-to-RGB conversion.

Note that relying on a Fourier transform as in the method of Belcour and Barla [BB17] is not relevant since the Fourier transform of a Bragg mirror spectrum is as complex as the spectrum itself, which is mainly due to the presence of band gaps that produce high-frequency oscillations in Fourier space.

3.2.1. Spectral landmarks

We start by assuming that the number N of cells is sufficiently large to achieve a reflectance of 95% in the BG. so that we may approximate the reflectance spectrum by its envelope R_ω^e (gray spectrum in Figure 3) – see [Yeh88] :

$$R_\omega^e = \frac{|C|^2}{|C|^2 + (\sin K\Lambda)^2}. \tag{11}$$

In the following, we use $\omega = \frac{2\pi}{\lambda}$ instead of λ because it can be observed in Equation 8 that it has a linear relation to Λ through the k_{1z} and k_{2z} terms. Intuitively, scaling Λ has the effect of compressing or stretching the reflected spectrum of a Bragg mirror along ω. This can be observed in Figure 4 where more band gaps and oscillations appear in the visible range when increasing Λ.

As illustrated at the bottom of Figure 3, *band gap edges* are located where the dispersion relation obeys $|\cos K\Lambda| = 1$ (green dots) ; inside pairs of such landmarks, $R_\omega^e = 1$. Since the dispersion relation oscillates between positive and negative maxima, it goes through zero inbetween each band gap. We call these spectral locations *Airy points* (cyan dots) since when $\cos K\Lambda = 0$, we have $R_\omega^e = |r_1|^2$, with r_1 the Airy reflection coefficient of Equation 10.

To the best of our knowledge, neither band gap edges nor Airy points can be located analytically. We thus rely on an accurate numerical approach to find these landmarks, described below. A final set of landmarks consists in the *zero points* of R_ω^e (black dot), which occur when $r_1 = 0$, since then $|C|^2 = 0$, and are given by :

$$\omega_z = \frac{z\pi}{n_2 \cos\theta_2 d_2} \quad \text{with} \quad z \in \mathbb{N}^+, \tag{12}$$

observing that the numerator of Equation 10 vanishes when $\phi = z\pi$. Aside from zero points, spectral landmarks depend on polarization.

Dispersion landmarks. The key idea for finding dispersion landmarks is to first identify special locations ω_m that we call *modes* (red crosses in Figure 3). They lie inside each band gap and provide a structure for landmark search. As detailed in Appendix A,
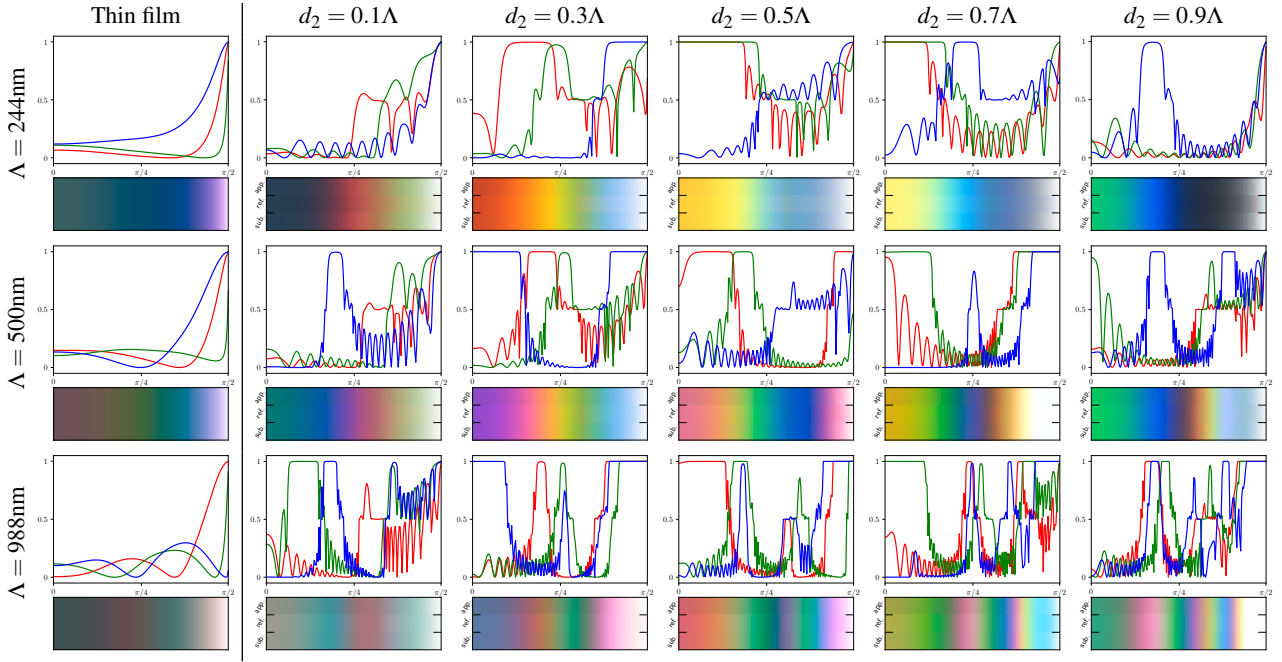
FIGURE 4 – *An exploration of the set of angular color gradients produced by Bragg mirrors of indices $n_1 = 1$ and $n_2 = 1.5$, period Λ varying per row, and relative thicknesses d_1 and d_2 varying per column (with $\Lambda = d_1 + d_2$), using $N = 20$ repetitions. The first column shows the case of a thin-film slab of index $n = 1.5$ in air, its thickness Λ varying per row. The plots show reflectance as a function of the incidence angle for three wavelengths corresponding to the CMF peaks ($\lambda = \{559, 556, 442\}$nm for red, green and blue respectively). As expected, more oscillations appear with increasing Λ. Below each plot we show color gradients obtained from the ground truth (ref.), and in the case of Bragg mirrors, using our basic (app.) or subdivided (sub.) approximation. Both methods yield close approximations, the latter being slightly more accurate in terms of luminance. Compared to thin films, Bragg mirrors exhibit much more vivid and diverse color gradients.*

spectral modes are given by :

$$\omega_m = \frac{m\pi}{n_1 \cos\theta_1 d_1 + n_2 \cos\theta_2 d_2} \quad \text{with} \quad m \in \mathbb{N}^+, \quad (13)$$

with even (resp. odd) m corresponding to a positive (resp. negative) dispersion relation. We use a dichotomy between pairs of modes to find the 0-crossings of $\cos K\Lambda$, yielding Airy points ω_a. Band gap edges ω_b are also found via dichotomy, this time between contiguous $\{\omega_m, \omega_a\}$ or $\{\omega_a, \omega_m\}$ pairs. Finally, we insert the zero points ω_z when they lie inbetween a $\{\omega_b, \omega_a\}$ or $\{\omega_a, \omega_b\}$ pair. This process results in an ordered list $\{\omega_j\}$ of spectral landmarks. In practice, we only consider those that overlap the visible range.

3.2.2. Piecewise-constant spectra

We now use spectral landmarks to approximate the spectral reflectance by a piecewise-constant formulation $\tilde{R}_\omega = \sum_j w_j B_j(\omega)$ (dashed red curve in Figure 3), where w_j are coefficients and B_j are box functions with boundaries aligned with spectral landmarks :

$$B_j(\omega) = H(\omega - \omega_j) - H(\omega - \omega_{j+1}), \quad (14)$$

with H the Heaviside function. For the basis coefficients, we have $w_j = 1$ inside band gaps by construction since $R_\omega^e = 1$. We also rely on the envelope outside of band gaps, which has the advantage of avoiding instabilities since the envelope is oscillation-free. In practice, we use $w_j = \tilde{w}(\theta) R_\omega^e \left(\frac{\omega_j + \omega_{j+1}}{2} \right)$. The angular correction term

$\tilde{w}$ (see Appendix B) is used to compensate for the higher intensity of the envelope compared to the ground truth spectrum.

Converting a reflectance spectrum to a RGB spectrum first requires to integrate the former over color matching functions (CMFs) to yield a XYZ color. Writing $\bar{\mathbf{c}}(\omega) = [\bar{x}(\omega), \bar{y}(\omega), \bar{z}(\omega)]^T$ the vector of CMFs, we obtain the approximate XYZ reflectance :

$$\begin{aligned} \tilde{\mathbf{R}} &= \int \tilde{R}_\omega \bar{\mathbf{c}}(\omega) d\omega \\ &= \sum_j w_j \left(\bar{\mathbf{C}}(\omega_{j+1}) - \bar{\mathbf{C}}(\omega_j) \right), \quad (15) \end{aligned}$$

with $\bar{\mathbf{C}} = [\bar{X}, \bar{Y}, \bar{Z}]^T$ the vector of cumulative integrals of CMFs :

$$\bar{\mathbf{C}}(\omega_{max}) = \int_0^{\omega_{max}} \bar{\mathbf{c}}(\omega) d\omega = 1 - \int H(\omega - \omega_{max}) \bar{\mathbf{c}}(\omega) d\omega. \quad (16)$$

The $\bar{X}$, $\bar{Y}$ and $\bar{Z}$ cumulative integrals are computed *only once* in pre-process. At runtime, we evaluate Equation 15 by performing one lookup in tabulated cumulative integrals per spectral landmark. Since landmarks depend on polarization, separate XYZ approximations must be computed for each polarization, and then averaged together. The resulting XYZ color is finally converted to a RGB color using classic colorimetric formula.

Approximation quality. The proposed piecewise-constant approximation yields accurate results in terms of chromaticity, as

shown in the color gradients (app.) of Figure 4. However, it might be slightly off in terms of luminance, depending on the location and number of band gaps in the visible spectrum. When most of the band gaps are outside the spectrum, the piecewise-constant approximation of the envelope between band gaps may be too crude.

To remedy this, we optionally subdivide boxes outside of band gaps. Due to the linear relationship between Λ and ω, the space outside of band gaps showing in the visible spectrum will likely be larger for the first modes. Since each box can be related to a mode number m, we subdivide them into $\max(1, s - m)$ sub-boxes, where $s \in \mathbb{N}^+$ is a user-controlled quality parameter (we use $s = 3$ in all our examples). As shown in the color gradients (sub.) of Figure 4, this *subdivided* version mostly corrects luminance inaccuracies. Some slight differences with the reference remain at low Λ values. One could think that a closer approximation would be obtained with a piecewise-linear instead of a piecewise-constant approximation; However, as demonstrated in supplemental material, such an approach does not yield better results and is less efficient. We evaluate the performance of our approximations in Section 5.

4. Layered Bragg Structures

A material made of a single Bragg mirror looks like a colored smooth surface. Many examples of naturally iridescent materials exhibit a rougher look due to microscopic irregularities (see Figure 2(b)) that scatter light. We mimic such material appearance using a layered structure of Bragg mirrors distributed across a range of orientations (Section 4.1). We then describe how such a structure may be rendered using a position-free approach (Section 4.2), and show that transmission is ballistic in our case. This not only speeds up the rendering process, but also lets us introduce an efficient single-reflection BRDF model (Section 4.3).

4.1. Hypothesis

We consider a layered micro-structure, where each layer is made of a distribution of identical Bragg mirrors with different orientations, which we call a *rough Bragg layer*. In natural materials, photonic crystals are often layered on a pigmented background, which is usually dark (e.g., melanin) to increase the contrast of iridescent colors. We mimic this configuration by adding a diffuse base layer of reflectance ρ_D. Figure 2(e) illustrates such a micro-structure.

We assume that the distribution of orientations in a rough Bragg layer does not induce interference effects (e.g., no diffraction). As a result, we model the BSDF of a Bragg layer using microfacet theory [TS67]. The BRDF is obtained by replacing the Fresnel reflectance term by the Yeh reflectance R_λ of Section 3.1 :

$$f_r(\mathbf{i}, \mathbf{o}) = \frac{D(\mathbf{h})G(\mathbf{i}, \mathbf{o}, \mathbf{h})R_\lambda(\mathbf{i}.\mathbf{h})}{4|\mathbf{i}.\mathbf{n}||\mathbf{o}.\mathbf{n}|}, \qquad (17)$$

where $\mathbf{h} = \frac{\mathbf{i}+\mathbf{o}}{|\mathbf{i}+\mathbf{o}|}$ is the halfway vector between the ingoing and outgoing directions $\mathbf{i}$ and $\mathbf{o}$, and $\mathbf{n}$ is the geometric normal. We use the isotropic Trowbridge-Reitz (GGX) distribution throughout, given for an arbitrary microfacet normal $\mathbf{m}$ by [TR75, WMLT07] :

$$D(\mathbf{m}) = \frac{\alpha^2 \chi^+(\mathbf{m}.\mathbf{n})}{\pi \cos^4 \theta_m (\alpha^2 + \tan^2 \theta_m)^2} \qquad (18)$$

with $\alpha \in [0, 1]$ the roughness parameter and χ^+ the Heaviside function. The corresponding geometric attenuation factor is given by $G(\mathbf{i}, \mathbf{o}, \mathbf{m}) = G_1(\mathbf{i}, \mathbf{m})G_1(\mathbf{o}, \mathbf{m})$, with :

$$G_1(\mathbf{i}, \mathbf{m}) = \chi^+\left(\frac{\mathbf{i}.\mathbf{m}}{\mathbf{i}.\mathbf{n}}\right) \frac{2}{1 + \sqrt{1 + \alpha^2 \tan^2 \theta_i}}. \qquad (19)$$

The BTDF has a special form, as detailed in Section 4.2 : since each Bragg mirror is embedded in a host medium of index n_1, the transmitted rays are not scattered or even refracted through a rough Bragg layer. In other words, the BTDF is *ballistic*.

When $n_1 \neq 1$, we add a smooth coating on top of the structure, as in Figure 2(e). The case $n_1 = 1$ maximizes the refractive index contrast, yielding the most vivid colors. Even though it might sound like a departure from physical realism, similar configurations are found in nature, such as in the Morpho butterfly where a Bragg mirror is held by a central micro-pillar. We consider that there is no absorption nor scattering in the host medium, and that it is thick enough so that interference effects among different layers can be neglected. Likewise, polarisation effects among layers are ignored, which is likely to be a valid assumption in our case [WWHN17].

4.2. Monte-carlo simulation

A straightforward solution to render a layered Bragg structure is to rely on position-free forward Monte-Carlo light transport in the layered structure (e.g., [GHZ18, GGN20]). This requires to properly transmit light rays through rough Bragg layers.

4.2.1. Ballistic transmission

Rays impinging on a rough Bragg layer are transmitted in the same direction irrespective of roughness since it is bounded by the same host medium on either side. The exit point on transmission is laterally offset, but this is ignored in a position-free framework.

As a result, the BTDF of a Bragg layer has a special form. We start from the general formulation of Walter [WMLT07] :

$$f_s(\mathbf{i}, \mathbf{o}) = \int_\Omega \left|\frac{\mathbf{i}.\mathbf{m}}{\mathbf{i}.\mathbf{n}}\right| \left|f_s^m(\mathbf{i}, \mathbf{o}, \mathbf{m})\right| \left|\frac{\mathbf{o}.\mathbf{m}}{\mathbf{o}.\mathbf{n}}\right| G(\mathbf{i}, \mathbf{o}, \mathbf{m})D(\mathbf{m})d\omega_m, \quad (20)$$

where $f_s^m(\mathbf{i}, \mathbf{o}, \mathbf{m})$ denotes the micro-BSDF of the microfacet oriented in the direction $\mathbf{m}$. The BTDF of Walter et al. [WMLT07] assumes that each microfacet transmits in the specular direction.

$$f_t^m(\mathbf{i}, \mathbf{o}, \mathbf{m}) = T_\lambda(\mathbf{i}, \mathbf{m})\frac{\delta_{\omega_o}(\mathbf{s}_\eta(\mathbf{i}, \mathbf{m}), \mathbf{o})}{|\mathbf{o}.\mathbf{m}|} \qquad (21)$$

with $\mathbf{s}_\eta(\mathbf{i}, \mathbf{m})$ the specularly refracted direction of $\mathbf{i}$ across the interface of normal $\mathbf{m}$ and refractive index ratio η; and δ_{ω_o} a Dirac delta function whose value is infinite when $\mathbf{s}_\eta = \mathbf{o}$ and zero otherwise. Note that we use Equation (9) of the work of Walter et al. [WMLT07], instead of their Equation (11), which would be undefined in our case since the halfway vector in transmission is not defined when $\mathbf{o} = -\mathbf{i}$.

In the ballistic case, we have instead $\mathbf{s}_1(\mathbf{i}, \mathbf{m}) = -\mathbf{i}$ for all incoming directions $\mathbf{i}$ and micronormals $\mathbf{m}$. Plugging this special configuration in Equation 21 then Equation 20, we obtain the ballistic
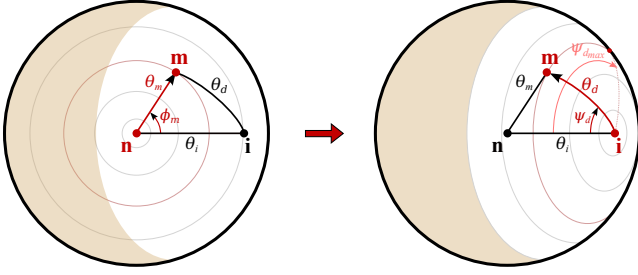
FIGURE 5 – *We express a microfacet normal* **m** *with respect to the ingoing direction* **i** *with a change of variable. Configurations where* $\mathbf{i} \cdot \mathbf{m} < 0$ *are shown in beige. The integral along* ψ_d *must be restricted to* $[-\psi_{d_{max}}, \psi_{d_{max}}]$ *to ensure that* $\mathbf{m} \cdot \mathbf{n} \geq 0$.

(a) $\alpha = 0.1$ (b) $\alpha = 0.4$

FIGURE 6 – *Plots of the transmission filter as a function of* θ_d *for two roughness values (a,b), at three incidence angles* $\theta_i \in \{\frac{\pi}{32}, \frac{\pi}{4}, \frac{7\pi}{16}\}$. *The vertical axes differ between plots. The filter is usually skewed and not centered on* θ_i. *It decreases in intensity for an increasing* θ_i. *A* $\mathcal{C}^1$ *discontinuity occurs at* $\theta_d = \frac{\pi}{2} - \theta_i$ *(see Equation 26), and is best seen for* $\alpha = 0.4$ *(orange Arrow).*

BTDF after a few simplifications :

$$f_t(\mathbf{i}, \mathbf{o}) = \delta_{\omega_o}(-\mathbf{i}, \mathbf{o}) \int_\Omega \frac{|\mathbf{i}.\mathbf{m}|}{|\mathbf{i}.\mathbf{n}|^2} T_\lambda(\mathbf{i}, \mathbf{m}) G(\mathbf{i}, -\mathbf{i}, \mathbf{m}) D(\mathbf{m}) d\omega_m. \tag{22}$$

4.2.2. Integrated transmissivity

In the context of a position-free Monte-Carlo simulation, we need to evaluate $f_t(\mathbf{i}, -\mathbf{i}, \mathbf{n}) |\mathbf{i}.\mathbf{n}|$, the BTDF in the ballistic direction multiplied by the cosine term. If we assume that the incoming light direction is incident from above (i.e., $\mathbf{i}.\mathbf{n} = \cos\theta_i \geq 0$) and with an isotropic distribution D, we may re-express Equation 22 in terms of zenithal and azimuthal angles :

$$f_t(\theta_i) \cos\theta_i =$$
$$\int_0^{2\pi} \int_0^{\frac{\pi}{2}} \frac{\cos\theta_d}{\cos\theta_i} T_\lambda(\theta_d) G(\theta_i, \theta_m, \phi_m) D(\theta_m) \sin\theta_m d\theta_m d\phi_m, \tag{23}$$

where we have introduced the difference angle $\theta_d = \cos^{-1}(\mathbf{i}.\mathbf{m})$.

Even in the isotropic case, Equation 23 remains complex to evaluate, and it must be recomputed whenever a parameter of a Bragg layer is modified. However, aside from α, all parameters solely affect the spectral transmissivity T_λ, which only depends on θ_d. We thus perform a change of variable : we rotate the spherical domain of integration to align **i** with **n**. As a result (see Figure 5), we have :
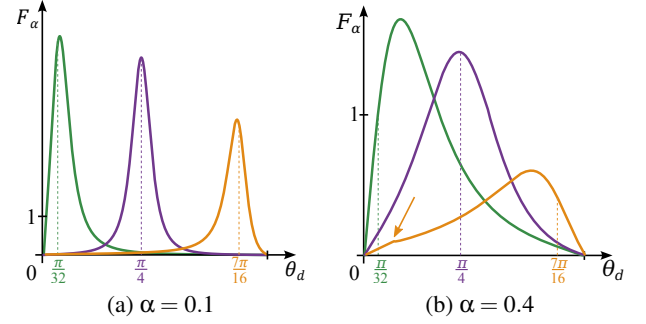
$$\theta_m(\theta_i, \theta_d, \psi_d) = \arccos(\cos\theta_i \cos\theta_d + \sin\theta_i \sin\theta_d \cos\psi_d), \tag{24}$$

which we simply write θ_m for concision. Equation 23 becomes :

$$f_t(\theta_i) \cos\theta_i = 2 \int_0^\pi \int_0^{\frac{\pi}{2}} \frac{\cos\theta_d}{\cos\theta_i} T_\lambda(\theta_d) G_1^2(\theta_i) D(\theta_m) \sin\theta_d d\theta_d d\psi_d, \tag{25}$$

where the prefactor of 2 is due to the symmetry of θ_m with respect to ψ_d (see Equation 24 and Figure 5), and the geometric attenuation factor becomes $G_1^2(\theta_i)$ in this case. Note that the χ^+ term of Equation 19 (beige region in Figure 5) then vanishes since we have $\theta_d \in [0, \frac{\pi}{2}]$ in Equation 25.

If we rewrite Equation 18 as $D(\theta_m) = \chi^+(\cos\theta_m) \tilde{D}(\theta_m)$, we may explicitly derive the bounds of the outer integral in Equation 25. Indeed, using Equation 24, we find that imposing $\cos\theta_m \geq$

0 is equivalent to imposing $\psi_d \leq \psi_{d_{max}}(\theta_i, \theta_d)$ (see Figure 5), with :

$$\psi_{d_{max}}(\theta_i, \theta_d) = \begin{cases} \arccos\left(-\frac{1}{\tan\theta_i \tan\theta_d}\right) & \text{if } \theta_d + \theta_i \geq \frac{\pi}{2}, \\ \pi & \text{otherwise.} \end{cases} \tag{26}$$

As a result, we obtain :

$$f_t(\theta_i) \cos\theta_i =$$
$$2 \int_0^{\pi/2} \int_0^{\psi_{d_{max}}} \frac{\cos\theta_d}{\cos\theta_i} T_\lambda(\theta_d) G_1^2(\theta_i) \tilde{D}(\theta_m) \sin\theta_d d\psi_d d\theta_d, \tag{27}$$

which we rewrite as a 1D integral :

$$f_t(\theta_i) \cos\theta_i = \int_0^{\pi/2} T_\lambda(\theta_d) F_\alpha(\theta_i, \theta_d) d\theta_d, \tag{28}$$

where F_α is a roughness-dependent 2D filtering function :

$$F_\alpha(\theta_i, \theta_d) = 2 G_1^2(\theta_i) \frac{\cos\theta_d}{\cos\theta_i} \int_0^{\psi_{d_{max}}} \tilde{D}(\theta_m) \sin\theta_d d\psi_d. \tag{29}$$

For an incoming light direction incident from below, we simply consider that the geometric normal of the Bragg layer is flipped.

Equation 28 explicitly shows that the ballistic BTDF is a weighted combination of transmissivities of Bragg mirrors at various difference angles θ_d, with weights determined by the filter function F_α. As shown in Figure 6, F_α widens with increasing roughness α. Moreover, it is not centered on θ_i, and exhibits a skewed shape except when $\theta_i = \frac{\pi}{4}$. As a result, the color saturation and hue of a rough Bragg layer is modified compared to a smooth Bragg layer with identical indices and thicknesses. The intensity also decreases, which is due to the G_1 term in Equation 29.

Such a formulation is not only useful to understand how transmitted spectra are affected by roughness and angle of incidence, but it may also be used to speed up the computation of the ballistic BTDF, which we refer as our *optimized* simulation. For a given α, we precompute, once and for all, a 2D lookup table (approx. 1.4 MB) for $F_\alpha(\theta_i, \theta_d)$ by evaluating the 1D integral of Equation 29. We use uniform sampling in the θ_i dimension, and non-uniform

sampling in the θ_d dimension (via a sampling of the GGX distribution). Then for a Bragg layer, we precompute on the CPU a 1D table (approx. 620KB) for the integrated transmissivity defined in Equation 28 (instead of the 2D integral of Equation 23).

.

4.2.3. Importance sampling

The last required ingredient for rendering layered Bragg structures is the probability that a light path is transmitted through a Bragg layer. Even though we have $R_\lambda + T_\lambda = 1$ for a Bragg mirror, this does not extend to *rough* Bragg layers since we do not handle multiple scattering among microfacets in our approach. A rough Bragg layer thus absorbs a part A of the incoming light, which is obtained from Equation 28 by assuming $T_\lambda = 1$:

$$A(\theta_i) = 1 - \int_0^{\frac{\pi}{2}} F_\alpha(\theta_i, \theta_d) d\theta_d = 1 - G_1(\theta_i), \quad (30)$$

where the last equality is derived in Appendix C.

In order to balance out the sampling of reflection and transmission, we need to account for half of the absorption in each case. The probability of transmission through a Bragg layer at an angle θ_i and for a specific wavelength λ is then given by :

$$p_{\text{trans}}(\theta_i) = \frac{f_t(\theta_i)\cos\theta_i}{1 - \frac{A(\theta_i)}{2}} = 2\frac{\int_0^{\pi/2} T_\lambda(\theta_d) F_\alpha(\theta_i,\theta_d) d\theta_d}{1 + G_1(\theta_i)}, \quad (31)$$

with the corresponding wavelength-independent weight given by :

$$\text{weight}(\theta_i) = 1 - \frac{A(\theta_i)}{2} = \frac{1 + G_1(\theta_i)}{2}. \quad (32)$$

Up until now, we have assumed that all wavelengths are handled separately. However, since there is no dispersion in layered Bragg structures, we may use a *multiplexed* implementation, whereby each light path caries out all wavelengths at once. The probability of transmission p_{trans} is then given by Equation 31 with the only difference that the numerator is replaced by $\langle f_t(\theta_i)\cos\theta_i \rangle_\lambda$, with $\langle \cdot \rangle_\lambda$ the average over wavelengths. The weight of a sample obtained with this PDF is now wavelength-dependent :

$$\text{weight}(\theta_i) = \frac{1 + G_1(\theta_i)}{2} \frac{f_t(\theta_i)\cos\theta_i}{\langle f_t(\theta_i)\cos\theta_i \rangle_\lambda} \quad (33)$$

We validate our optimized simulation against a Monte-Carlo reference simulation in Supplemental material.

4.3. Single-reflection BRDF model

We now exploit the specific ballistic transmission of a Bragg layer to derive an analytical formula for the evaluation of a single-reflection BRDF. This approximate spectral model only considers the light paths that have reflected *once* on *any* of the layers.

4.3.1. BRDF evaluation

The single-reflection BRDF is given by :

$$f_r(\mathbf{i}, \mathbf{o}) = f_{r,0}(\mathbf{i}, \mathbf{o}) + \frac{1}{n_1^2} \sum_{l=1}^{L} f_{r,l}(\mathbf{i}, \mathbf{o}) \left(\prod_{k=0}^{l-1} f_{t,k}(\mathbf{i}) f_{t,k}(\mathbf{o}) \right), \quad (34)$$

where L is the number of layers (not including the optional smooth coating), $f_{r,l}$ and $f_{t,l}$ denote the BRDF and BTDF of the lth layer, and $\mathbf{i}$ and $\mathbf{o}$ denote the *refracted* incoming and outgoing vectors, except when they are used to evaluate $f_{r,0}$ or $f_{t,0}$. When $n_1 = 1$, we have $f_{r,0} = 0$, $f_{t,0} = 1$, and the incoming and outgoing directions are never refracted.

Equation 34 is fast to evaluate thanks to the integrated transmissivity introduced in Section 4.2.2, which we use to obtain the $f_{t,k}$ terms. As opposed to the simulation of the previous section, it can be directly evaluated for a pair of ingoing and outgoing directions, which we use for next event estimation (e.g., as in Figure 11).

4.3.2. Importance sampling

When sampling the single-reflection model, one first needs to determine the probability of the lth layer to be the one onto which reflection occurs. It is given by :

$$p_{\text{refl}_l}(\theta_i) = \left(1 - p_{\text{trans}_l}(\theta_i) \right) \prod_{k=0}^{l-1} p_{\text{trans}_k}(\theta_i), \quad (35)$$

where p_{trans_k} is given by Equation 31.

Figure 7 compares our single-reflection BRDF model to the reference simulation. Slight intensity differences show up when Bragg layers are laid on a bright diffuse base ; otherwise, the approximation of our model is very good. In supplemental material, we validate our model against a Monte-Carlo reference simulation where we only consider single-reflection paths.

5. Results and discussion

In this section, we first evaluate the performance gains of our RGB approximation and single-reflection BRDF model. We then explore the appearance space of layered Bragg structures, and discuss its relationships to other iridescent structures.

Performance evaluation Our RGB approximation allows one to quickly explore the appearance of a Bragg mirror, as was already shown in Figure 4. In Figure 8, we perform a similar comparison on a single *rough* Bragg layer, for different roughness values. Our basic approximation already yields faithful color fringes, but slight intensity differences remain. With our subdivided approximation (using $s = 3$), results get closer to the reference, while still providing significant performance speedups. In the supplemental video, we provide a live demonstration of our model, implemented as a shader inside BRDF Explorer. The impact of the number s of subdivisions on rendering accuracy is detailed in supplemental material, where we show that $s = 3$ is a good trade-off between speed and accuracy. As summarized in Table 1, performance depends fundamentally on the Λ parameter : for higher values of Λ, more BG are found in the visible range, which requires more basis functions and weights evaluations. However, most of the interesting iridescent effects are achieved when Λ is below a micron, in which case our basic and subdivided approximations can be respectively up to ten and five times faster than the reference.

Our single-reflection model is compared to a simulation that only involves single-reflection paths (SR sim.) in Table 2. We use a

| *A* on diffuse | *A* on *B* | *A* on *B* on diffuse | *A′* under smooth coating |
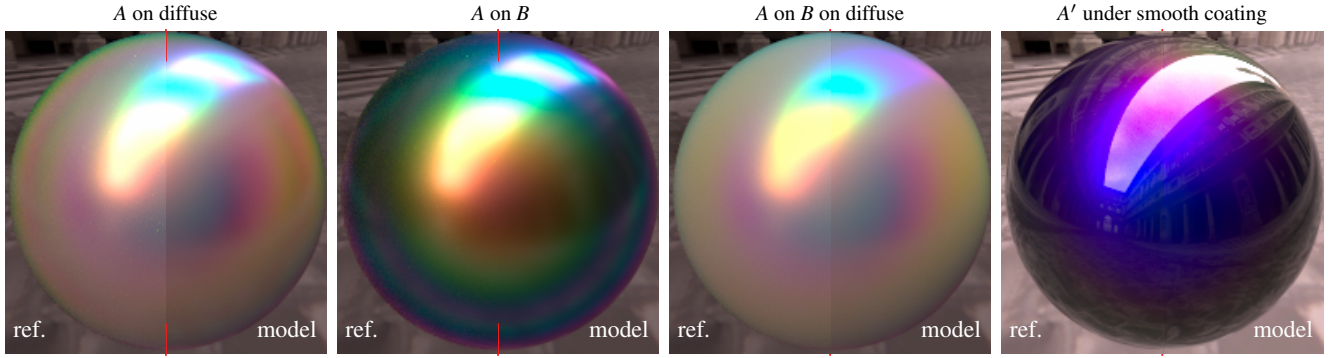
FIGURE 7 – *Comparisons of a reference light transport in four layered Bragg structures (columns) with our single-reflection BRDF model on a sphere placed in the* Uffizi Gallery *environment map. We use $n_1 = 1$, $n_2 = 1.5$ and $N = 10$ in the first three columns, with two Bragg configurations : A ($d_1 = d_2 = 250nm$, $\alpha = 0.1$) and B ($d_1 = d_2 = 494nm$, $\alpha = 0.05$). The last column uses A', a modified version of A with $n_1 = 1.35$ (i.e., under a smooth coating). Visual differences occur in the presence of a diffuse base ($\rho_d = 0.5$), as it tends to raise the proportion of light paths that undergo multiple reflections. For the model, the filter $F_\alpha(\theta_i, \theta_d)$ is precomputed using 1000 samples for ψ_d with a resolution of $0.25°$ for both θ_i and θ_d. This computation takes approximately 0.5 seconds on an Intel Core i7-9700k 3.60GHz CPU.*
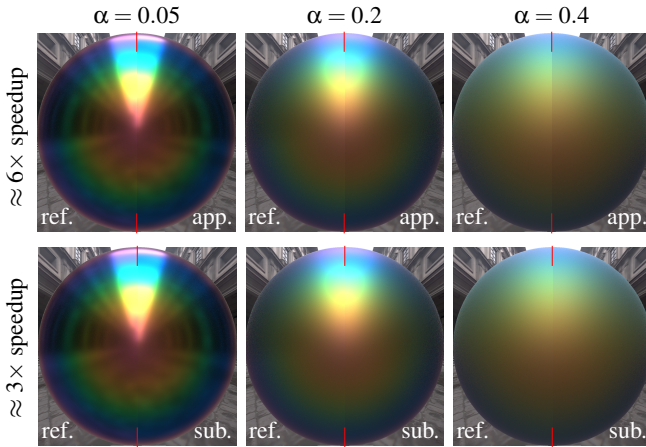
FIGURE 8 – *Comparisons of our two RGB approximations (rows) to the reference when rendering a Bragg layer ($n_1 = 1$, $n_2 = 1.5$, $\Lambda = 500nm$, $d_1 = d_2 = 0.5\Lambda$) with three different roughness values (columns). The subdivided approximation (sub., using $s = 3$) yields more accurate results in this case, while still providing a reasonable speed-up, which is roughly independent of α.*

Λ	app.	sub. (s=2)	sub. (s=3)	sub. (s=4)	sub. (s=5)
244nm	×10.6	×8.8	×5.5	×4.5	×3.8
500nm	×6.8	×5.0	×3.5	×2.6	×2.1
988nm	×4.2	×3.8	×3.1	×2.4	×1.7

TABLE 1 – *Performance speedups obtained with several versions of our RGB approximation, and for different values of Λ.*

	time (sec)	Avg. SMAPE	Eff.
SR sim.	$16-36-36$	$0.029-0.056-0.049$	$271-156-178$
Model	$14-15-15$	$0.016-0.031-0.024$	$570-692-882$
Model-LUT	$8.5-9.2-9.3$	$0.018-0.033-0.025$	$830-1044-1363$

TABLE 2 – *Comparisons of our single-reflection model with and without LUT against a single-reflection (SR) simulation, on the first three configurations of Figure 7, at $3Kspp$ and a 40×40 resolution. We use ground truth renderings at 30k spp at the same resolution to serve as references for SMAPE measurements. They take 127, 317 and 317 seconds respectively for each configuration.*

ground truth simulation involving all paths at $30K$ spp to serve as a reference when computing an average SMAPE metric :

$$SMAPE = \frac{1}{n}\sum_1^n \frac{|Ref_n - Model_n|}{(|Ref_n| + |Model_n|)/2}.$$

Our single-reflection model shows consistently better SMAPE for similar or smaller rendering times (i.e., it converges faster than the SR simulation). We have also implemented a version or our model where the Yeh reflectance term is stored in a LUT. It yields similar SMAPE values, but in significantly smaller times. In order to compare all three solutions, we use a measure of efficiency defined as $Eff = \frac{time_{GT}}{time \times Avg. SMAPE}$. Our single-reflection model exhibits a much better efficiency, in particular when using the LUT version.

Comparisons on reference scatterograms. As shown in Figure 2, some natural materials exhibit Bragg-like structures. In the case of the jewel beetle, three distinct regions are discernible on the cuticle, characterized by a green, a purple, and a red hue at normal incidence. These areas showcase Bragg-like structures with diverse parameters described in [SDGT11] and [SWS13]. All identified areas possess an epicuticle (approximately $1.3\mu m$ thick), composed of several layers with alternating high and low refractive indices. We use the parameters reported in Table 3 in our single-reflection spectral model using a single rough Bragg layer (of roughness 0.05) on top of an absorbing base. In this particular case, the host medium is air, which is different from either indices used in the Bragg mirror. We thus need to use a more general equation for reflectance, which we derive using Yeh's notations in Appendix D. Figure 9 compares scatterograms obtained with our model to scatterograms measured on a real jewel beetle [SWS13], showing qualitative agreement. Note that in principle, the ballistic transmission assumption is not
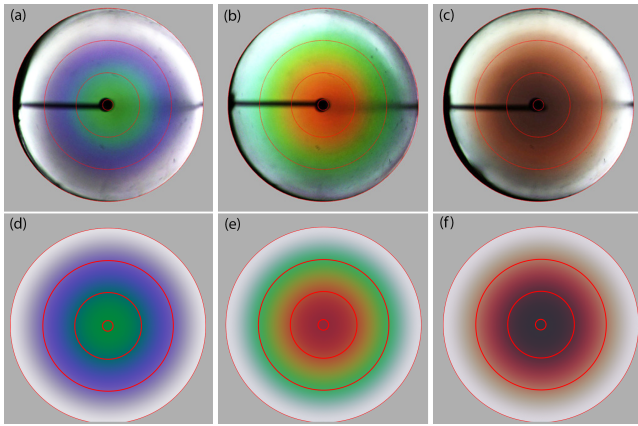
FIGURE 9 – *Top row : measured scatterograms of different areas of a jewel beetle cuticle [SWS13]. All images from Schenck et al. [SWS13] – © IOP Publishing, reproduced with permission, all rights reserved. Bottom row : spectral rendering of scatterograms using the physical properties of the insect's structures in our model. Our scatterograms are rendered using a hemispherical sensor camera in a white environnement. The red circles indicate angular reflection directions of* $5°$, $30°$, $60°$, *and* $90°$.

Area	n_1	n_2	Λ	δ	N
Green/Blue (a)	1.59	1.67	160	0.51	8
Red (b)	1.60	1.68	190	0.51	8
Purple (c)	1.60	1.68	205	0.51	6

TABLE 3 – *Parameters used for the cuticle areas in Figure 9.*

met when the host medium is not the same on either side of the Bragg layer. This is obviously not a problem when using an absorbing base. Even when using an arbitrary Lambertian base, our model remains valid since the distribution of transmitted rays does not matter in this case for the single-reflection approximation.

Appearance exploration A layered Bragg structure produces a rich variety of material appearance with vivid colors. Figure 1 shows a subset of them : using two different types of Bragg mirrors (here both with $n_1 = 1$), we show the effect of roughness on appearance, as well as a combination of a pair of Bragg layers, or of each individual layer on Lambertian bases (colored or achromatic). The supplemental video shows a live demonstration of our spectral single-reflection model, with interactive parameter editing.

In Figure 10, we explore more systematically the impact of two parameters. Appearance is very sensitive to the Bragg mirror period Λ : clearly visible differences appear with mere 30nm increments. The number N of repetitions mostly affects the saturation and intensity of colors. The effect is subtle when the host medium is air, but much more noticeable under a coating, in which case the refractive index contrast $\frac{n_2}{n_1}$ is reduced. In supplemental material, we render the diffuse component in isolation for the top two rows of Figure 10. This shows the effect of transmission through a Bragg layer, which yields angularly-varying color effects.

Figure 11 specifically shows the effect of varying the refractive

index contrast of a single Bragg layer : it not only affects the intensity of iridescent colors, but also changes the color fringes, as expected from Yeh's reflectance equations.

In Figure 12, we explore how appearance is affected by variations in roughness of different layered Bragg structures. The top and bottom rows show how color fringes are smoothed out as roughness is increased. The middle row shows a structure involving two Bragg layers, with the smoothest Bragg layer of the top row (framed) laid on top of Bragg layers of the bottom row. With increasing roughness of the bottom Bragg layer, a blue-shaded haze appears around reflections.

All spectral renderings have been made using the Malia Rendering Framework [mrf21], an open source library for predictive, physically-realistic rendering running on a desktop PC with a NVidia GeForce RTX 2080.

Relationship to other iridescent structures. There is a direct relationship between Bragg mirrors and thin-films. Indeed, when $N = 1$, Yeh's reflectance R_λ reduces to Airy's reflectance $|r_1|^2$. As shown in the left column of Figure 4, the corresponding spectra have much lower magnitudes since a higher N is required for band gaps to emerge. As a result, the color gradients are much less vivid.

Our approach bears some resemblance to the method of Guillén et al. [GMG*20], which involves iridescent flakes and a similar ballistic transmission. The two methods differ in two important respects though : their iridescent flakes rely on a few thin films involving complex refractive indices, and they use a volumetric description of the material structure. We have intentionally organized Figures 4 and 10 with a layout similar to Figures 3 and 11 in the work of Guillén et al. [GMG*20] to ease visual comparison. We first note that even though superficially similar color gradients may be obtained with the two methods, reflectance spectra differ substantially. In particular, with pearlescent flakes, there does not seem to be an equivalent to the mirror-like reflectance achieved inside band gaps. The appearance of pearlescent flakes in a binder also markedly differ from that of a rough Bragg layer in a host medium. Moreover, it varies according to different parameters : for instance, color saturation is controlled through flake density in their approach, while it is controlled by the number N of repetitions in ours. We thus believe the two methods should be treated as both structurally and qualitatively different.

6. Conclusion and future work

In this paper, we have introduced Yeh's equations for Bragg mirror reflectance, and explored the vivid iridescent color appearance they can produce. Our first contribution is an approximation to the reflectance spectrum, which helps explore the iridescent color appearance produced by different combinations of Bragg mirror parameters interactively. Our second contribution is an exploration of the appearance of rough layered Bragg structures, relying on microfacet theory (we chose to use the Trowbridge-Reitz(GGX) distribution, but any other distribution would work). Thanks to a pre-integrated ballistic transmission, we introduce an optimized position-free simulation and a fast single-reflection BRDF model.

Our main focus has been on the efficient exploration of *homogeneous* materials made of *isotropically*-distributed Bragg mirrors,
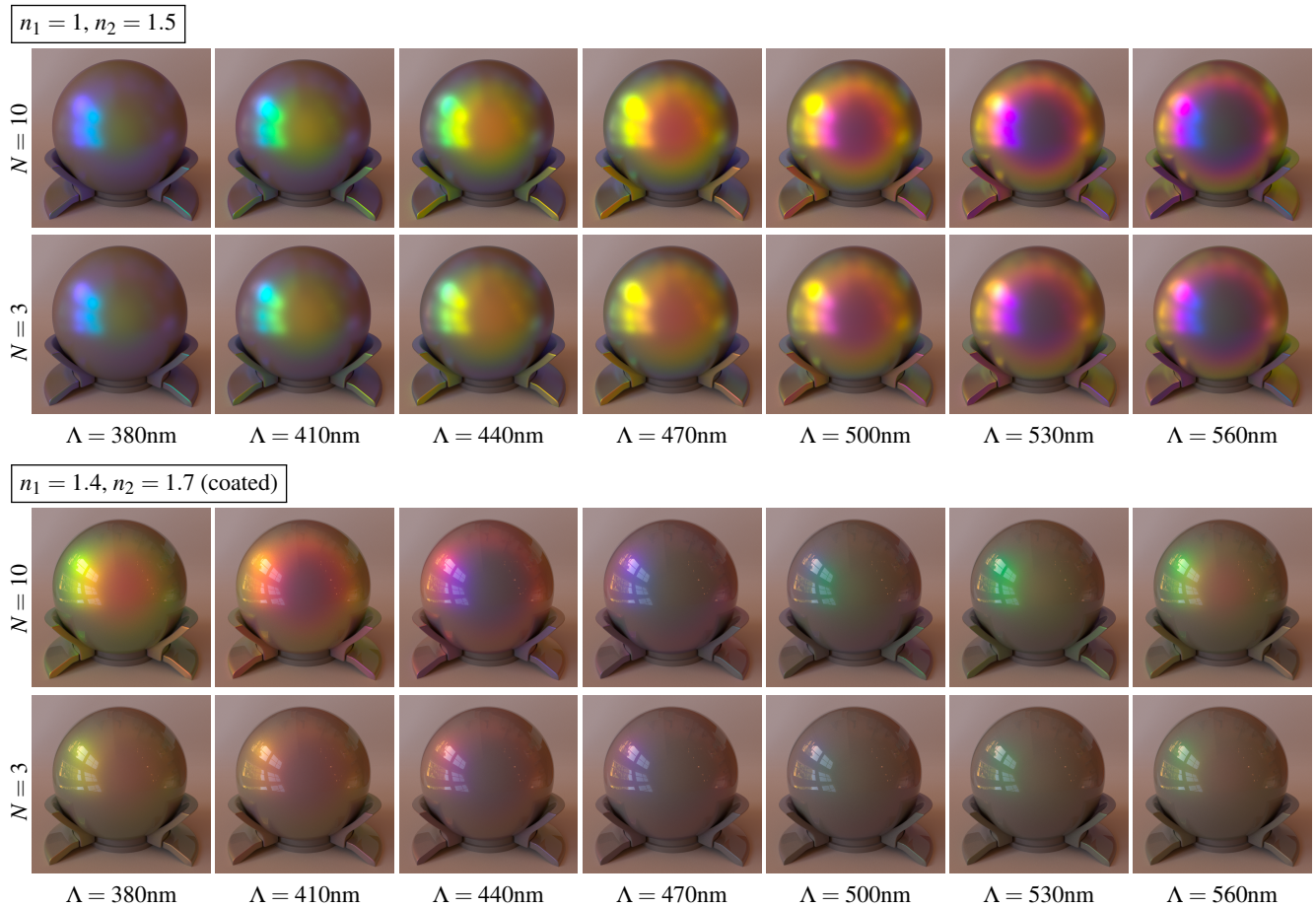
FIGURE 10 – *Exploration of the appearance of a single rough Bragg layer on top of a diffuse base, in air (top) or under a coating (bottom). In both cases, we use $\alpha = 0.1$, $\rho_d = 0.2$, $d_1 = 0.3\Lambda$ and $d_2 = 0.7\Lambda$, and we vary both Λ (horizontal axis) and N (vertical axis). Appearance is very sensitive to the value of Λ, as a mere increment of $30nm$ yields visible differences. The impact of N is more pronounced in the coated case than in air, which is due to the lower refractive index contrast. The probe is illuminated by* `At the Window (Wells, UK)` *environment map ©Bernhard Vog*

as demonstrated in the supplemental video. Extending our single-reflection BRDF model to spatially-varying materials will require to evaluate the transmission filter on the fly, in which case we will not be able to rely on the LUT version of the BRDF model. Dealing with anisotropic distributions will require extending the transmission filter itself to deal with the additional dimension. Note that these limitations do not apply to materials made of a single Bragg layer on top of an absorbing base, since transmission through the Bragg layer may then be disregarded. We show in Supplemental Material an example of a spatially-varying material of this type.

We would also like to investigate spectral sampling strategies as an alternative to spectral multiplexing, and we believe that our piecewise spectral approximation could be used in that respect. Another use of our spectral approximation would be in the inverse design of Bragg mirrors from target color gradients, an exciting topic for future work. Tone mapping and RGB gamut considerations might also be of interest since the vivid colors produced by Bragg mirrors often challenge reproduction on screens.

A limitation of our approach is that we do not consider multiple scattering among microfacets of a same layer, which is why we have limited roughness to $\alpha \leq 0.4$ in all of our results. It would be interesting to extend our approach to handle higher roughnesses. For instance, this could be done by combining our single-reflection model with recent advances in position-free simulation (e.g., [Bd22]). Another, perhaps even more challenging direction of future work would be to take into account irregularities that occur at scales comparable to visible wavelengths. As is visible in Figure 2, natural structures are not perfect Bragg mirrors. Modeling natural irregularities will likely require to take into account diffraction effects. In other instances, structural colors are combined with absorption and scattering in media to control iridescence. Even though absorption seems straightforward to add to our model (in media between Bragg layers), scattering will likely raise much more difficult issues (the layered model of Randrianandrasana et al. [RCL20] could open interesting solutions). Finally, other types of micro-structures are found in nature (2D or 3D photonic crystals, cholesteric structures). We thus believe that several modifications
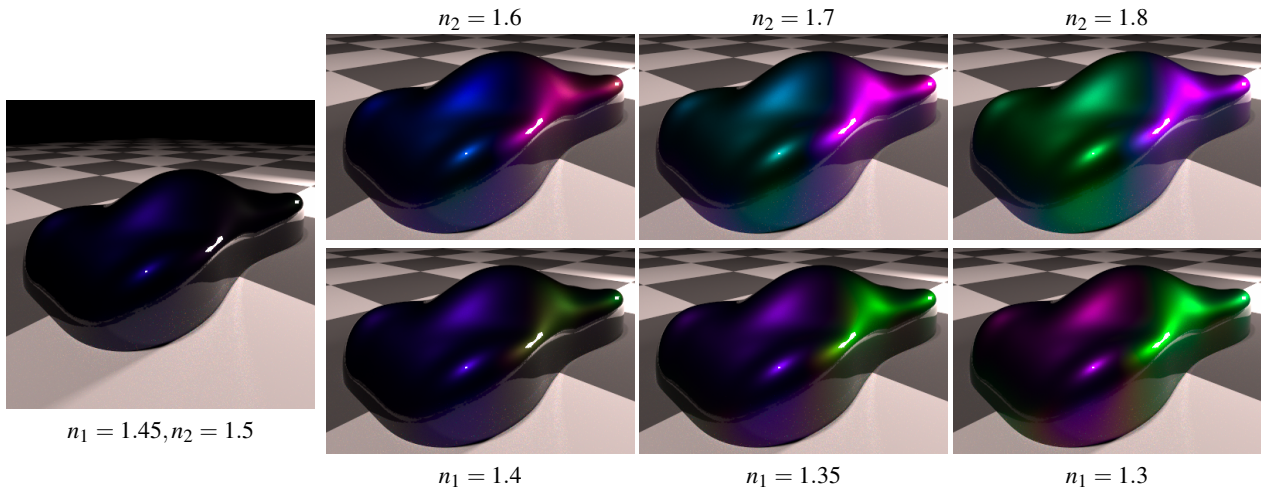
FIGURE 11 – *Variations of the refractive index contrast of a single Bragg layer ($d_1 = d_2 = 250nm$, $N = 20$, $\alpha = 0.1$). Starting in the leftmost configuration with a low refractive index ratio $\frac{n_2}{n_1}$, we either increase n_2 (top row) or decrease n_1 (bottom row) to increase the ratio, hence bringing in more iridescent color variations. The scene is only illuminated by two area ligths.*
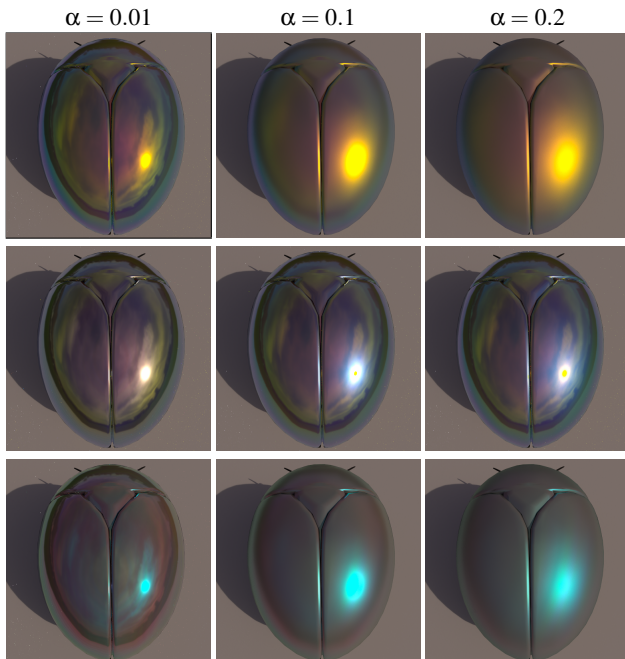
FIGURE 12 – *Variations of roughness (columns) in three layered Bragg structures, all using $n_1 = 1$, $n_2 = 1.5$, with a diffuse albedo $\rho_d = 0.2$. Top row : a single Bragg layer ($d_1 = 141nm$, $d_2 = 329nm$, $N = 3$). Bottom row : another single Bragg layer ($d_1 = 98nm$, $d_2 = 882nm$, $N = 10$). Middle row : the smoothest top Bragg layer (framed) laid onto each of the bottom Bragg layers. The scene is illuminated by the* `Green Point Park` *environment map featuring a bright sun and a cloudy sky.*

and extensions are necessary before we can tackle the ambitious goal of comparing to measured natural iridescent materials.

References

[BB17] BELCOUR L., BARLA P. : A practical extension to microfacet theory for the modeling of varying iridescence. *ACM Trans. Graph. 36*, 4 (jul 2017). doi:10.1145/3072959.3073620. 2, 4

[Bd22] BITTERLI B., D'EON E. : A Position-Free Path Integral for Homogeneous Slabs and Multiple Scattering on Smith Microfacets. *Computer Graphics Forum* (2022). doi:10.1111/cgf.14589. 11

[BP20] BENAMIRA A., PATTANAIK S. N. : Application of the transfer matrix method to anti-reflective coating rendering. In *Advances in Computer Graphics CGI, Proceedings* (2020), N. Magnenat-Thalmann e. a., (Ed.), vol. 12221 of *Lecture Notes in Computer Science*, Springer, Cham, pp. 83–95. doi:10.1007/978-3-030-61864-3_8. 2

[EKM01] ERSHOV S., KOLCHIN K., MYSZKOWSKI K. : Rendering pearlescent appearance based on paint-composition modelling. *Computer Graphics Forum 20*, 3 (2001), 227–238. doi:https://doi.org/10.1111/1467-8659.00515. 2

[EÖÖ16] ERGUN S., ÖNEL S., ÖZTÜRK A. : A general micro-flake model for predicting the appearance of car paint. In *EGSR (EI&I)* (2016), pp. 65–71. 2

[GAVH16] GUIDETTI G., ATIFI S., VIGNOLINI S., HAMAD W. Y. : Flexible photonic cellulose nanocrystal films. *Advanced Materials 28*, 45 (2016), 10042–10047. doi:https://doi.org/10.1002/adma.201603386. 2

[GCGP18] GUO J., CHEN Y., GUO Y., PAN J. : A physically-based appearance model for special effect pigments. *Computer Graphics Forum 37*, 4 (2018), 67–76. doi:https://doi.org/10.1111/cgf.13476. 2

[GGN20] GAMBOA L. E., GRUSON A., NOWROUZEZAHRAI D. : An efficient transport estimator for complex layered materials. *Computer Graphics Forum 39*, 2 (2020), 363–371. doi:https://doi.org/10.1111/cgf.13936. 6

[GHZ18] GUO Y., HAŠAN M., ZHAO S. : Position-free monte carlo simulation for arbitrary layered bsdfs. doi:10.1145/3272127.3275053. 6

[GMG*20] GUILLÉN I., MARCO J., GUTIERREZ D., JAKOB W., JARABO A. : A general framework for pearlescent materials. *ACM Trans. Graph. 39*, 6 (nov 2020). doi:10.1145/3414685.3417782. 2, 10

[GMN94] GONDEK J. S., MEYER G. W., NEWMAN J. G. : Wavelength dependent reflectance functions. In *Proceedings of the 21st Annual Conference on Computer Graphics and Interactive Techniques* (New York, NY, USA, 1994), SIGGRAPH '94, Association for Computing Machinery, p. 213–220. doi:10.1145/192161.192202. 2

[HKYM01] HIRAYAMA H., KANEDA K., YAMASHITA H., MONDEN Y. : An accurate illumination model for objects coated with multilayer films. *Computers & Graphics 25*, 3 (2001), 391–400. 2

[IA00] ICART I., ARQUÈS D. : A physically-based brdf model for multilayer systems with uncorrelated rough boundaries. In *Rendering Techniques 2000* (Vienna, 2000), Péroche B., Rushmeier H., (Eds.), Springer Vienna, pp. 353–364. 2

[IOS*09] IMURA M., OSHIRO O., SAEKI M., MANABE Y., CHIHARA K., YASUMURO Y. : A generic real-time rendering approach for structural colors. In *Proceedings of the 16th ACM Symposium on Virtual Reality Software and Technology* (New York, NY, USA, 2009), VRST '09, Association for Computing Machinery, p. 95–102. doi:10.1145/1643928.1643952. 2

[KGK19] KNEIPHOF T., GOLLA T., KLEIN R. : Real-time image-based lighting of microfacet brdfs with varying iridescence. *Computer Graphics Forum 38*, 4 (2019), 77–85. doi:https://doi.org/10.1111/cgf.13772. 2

[KK22] KNEIPHOF T., KLEIN R. : Real-time image-based lighting of metallic and pearlescent car paints. *Computers & Graphics 105* (2022), 36–45. doi:https://doi.org/10.1016/j.cag.2022.04.009. 2

[kWwZ15] KUN WU F., WEN ZHENG C. : Microfacet-based interference simulation for multilayer films. *Graphical Models 78* (2015), 26–35. doi:https://doi.org/10.1016/j.gmod.2014.12.003. 2

[MMRO13] MUSBACH A., MEYER G., REITICH F., OH S.-H. : Full wave modelling of light propagation and reflection. In *Computer Graphics Forum* (2013), vol. 32, Wiley Online Library, pp. 24–37. 2

[mrf21] The malia rendering framework. https ://gitlab.com/mrf-devteam/mrf/main.md.html, 2021. 10

[OZC*13] OKADA N., ZHU D., CAI D., COLE J. B., KAMBE M., KINOSHITA S. : Rendering morpho butterflies based on high accuracy nano-optical simulation. *Journal of Optics 42*, 1 (2013), 25–36. doi:10.1007/s12596-012-0092-y. 2

[RCL20] RANDRIANANDRASANA J., CALLET P., LUCAS L. : A six-flux transfer approach for efficient layered materials rendering. In *ACM SIGGRAPH 2020 Posters* (New York, NY, USA, 2020), SIGGRAPH '20, Association for Computing Machinery. doi:10.1145/3388770.3407453. 11

[Sch94] SCHLICK C. : An inexpensive brdf model for physically-based rendering. *Computer Graphics Forum 13*, 3 (1994), 233–246. doi:10.1111/1467-8659.1330233. 14

[SDGT11] STAVENGA D. G. WILTS BODO D. L. H. L., TAKAHIKO H. : Polarized iridescence of the multilayered elytra of the japanese jewel beetle, chrysochroa fulgidissima. *Philosophical Transactions of the Royal Society B : Biological Sciences 366*, 1565 (mar 2011), 709–23. doi:10.1098/rstb.2010.0197. 9

[SFDC00] SUN Y., FRACCHIA F. D., DREW M. S., CALVERT T. W. : Rendering iridescent colors of optical disks. In *Rendering Techniques 2000* (Vienna, 2000), Péroche B., Rushmeier H., (Eds.), Springer Vienna, pp. 341–352. 2

[SM92] SMITS B. E., MEYER G. W. : *Newton's Colors : Simulating Interference Phenomena in Realistic Image Synthesis.* Springer Berlin Heidelberg, Berlin, Heidelberg, 1992, pp. 185–194. doi:10.1007/978-3-662-09287-3_13. 2

[SMAS08] SHIOMI H., MISAKI E., ADACHI M., SUZUKI F. : High chroma pearlescent pigments designed by optical simulation. *Journal of Coatings Technology and Research 5*, 4 (2008), 455–464. doi:10.1007/s11998-008-9085-9. 2

[Sta99] STAM J. : Diffraction shaders. In *Proceedings of the 26th Annual Conference on Computer Graphics and Interactive Techniques* (USA, 1999), SIGGRAPH '99, ACM Press/Addison-Wesley Publishing Co., p. 101–110. doi:10.1145/311535.311546. 2

[Sta14] STAVENGA D. G. : Thin film and multilayer optics cause structural colors of many insects and birds. *Materials Today : Proceedings 1* (2014), 109–121. Living Light : Uniting biology and photonics – A memorial meeting in honour of Prof Jean-Pol Vigneron. doi:https://doi.org/10.1016/j.matpr.2014.09.007. 1

[Sun06] SUN Y. : Rendering biological iridescences with rgb-based renderers. *ACM Trans. Graph. 25*, 1 (jan 2006), 100–129. doi:10.1145/1122501.1122506. 2

[SW08] SUN Y., WANG Q. : Interference shaders of thin films. *Computer Graphics Forum 27*, 6 (2008), 1607–1631. doi:https://doi.org/10.1111/j.1467-8659.2007.01110.x. 2

[SWS13] SCHENK F., WILTS B. D., STAVENGA D. G. : The japanese jewel beetle : a painter's challenge. *Bioinspiration & Biomimetics 8*, 4 (nov 2013), 045002. doi:10.1088/1748-3182/8/4/045002. 4, 9, 10

[TR75] TROWBRIDGE T. S., REITZ K. P. : Average irregularity representation of a rough surface for ray reflection. *J. Opt. Soc. Am. 65*, 5 (May 1975), 531–536. doi:10.1364/JOSA.65.000531. 6

[TS67] TORRANCE K. E., SPARROW E. M. : Theory for off-specular reflection from roughened surfaces*. *J. Opt. Soc. Am. 57*, 9 (Sep 1967), 1105–1114. doi:10.1364/JOSA.57.001105. 6

[VPA*22] VYNCK K., PACANOWSKI R., AGREDA A., DUFAY A., GRANIER X., LALANNE P. : The visual appearances of disordered optical metasurfaces. *Nature Materials 21*, 9 (2022), 1035–1041. doi:10.1038/s41563-022-01255-9. 2

[WMLT07] WALTER B., MARSCHNER S. R., LI H., TORRANCE K. E. : Microfacet models for refraction through rough surfaces. In *Proceedings of the 18th Eurographics Conference on Rendering Techniques* (Goslar, DEU, 2007), EGSR'07, Eurographics Association, p. 195–206. 6

[WWHN17] WANG C., WILKIE A., HARCUBA P., NOVOSAD L. : Virtual ellipsometry on layered micro-facet surfaces. *Opt. Express 25*, 19 (Sep 2017), 22971–22990. doi:10.1364/OE.25.022971. 6

[Yeh88] *Optical waves in layered media.* New York (N.Y.) : Wiley, 1988., 1988. 1, 2, 3, 4, 14

[YLL*18] YANG B., LIU W., LI Z., CHENG H., CHEN S., TIAN J. : Polarization-sensitive structural colors with hue-and-saturation tuning based on all-dielectric nanopixels. *Advanced Optical Materials 6*, 4 (2018), 1701009. doi:https://doi.org/10.1002/adom.201701009. 2

Appendix A: Spectral mode landmarks

The identification of spectral landmarks relies on spectral modes. Here we prove that such landmarks always lie in a band gap.

We start by rewriting the dispersion relation of Equation 8 as :

$$\cos K\Lambda = (1 - \Theta)\cos n_-\omega + \Theta\cos n_+\omega, \tag{36}$$

with $n_{\pm}\omega = k_{1z}d_1 \pm k_{2z}d_2$, and $\Theta = \frac{1}{2}(1 + \frac{1}{2}\Omega)$. Observing that Ω is of the form $X + \frac{1}{X}$, we have $\Omega \geq 2$ since $X^2 - 2X + 1 \geq 0$, and thus $\Theta \geq 1$. We now consider the equation of a spectral mode,
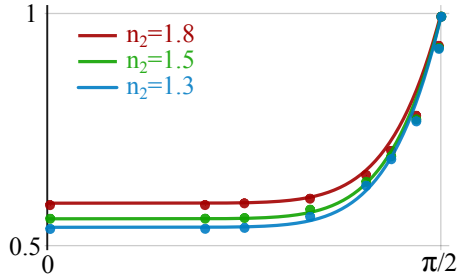
FIGURE 13 – *The approximate function $\tilde{w}(\theta_1)$ (solid curves) fits $w(\theta_1)$ (discrete dots) for three values of n_2, keeping $n_1 = 1$.*

$\omega_m = \frac{m\pi}{n_+}$, yielding $\cos K\Lambda = (1 - \Theta)\cos\frac{n_-}{n_+}\omega + \Theta(-1)^m$. For m even (resp. odd), it can be shown that we then have $\cos K\Lambda \geq 1$ (resp. $\cos K\Lambda \leq -1$). Hence ω_m is always inside a band gap.

It is interesting to note that at Brewster's angle (i.e., when $n_1\cos\theta_2 = n_2\cos\theta_1$), $\Omega_p = 2$ yielding $\cos K\Lambda = \cos n_+\omega$ for the 'p' polarisation. The Bloch wavenumber is thus real everywhere, and all the band gaps "close" at places where $|\cos K\Lambda| = 1$.

Appendix B: Angular correction term

As seen in Figure 3, a Bragg reflectance spectrum R_ω (in blue) converges toward its envelope R_ω^e (in grey) inside band gaps with increasing N. However, outside of band gaps, R_ω exhibits more oscillations with increasing N but does not exactly converges to R_ω^e.

Building our piecewise approximation exclusively on R_ω^e would thus tend to over-estimate the spectral reflectance outside of band gaps. We choose to correct for that intensity mismatch by using an angularly-dependent term in the basis weight formula. As a reference, we first compute the average ratio between the spectrum and its envelope outside of band gaps (i.e., for $K\Lambda \in [0, 2\pi]$) :

$$w(\theta_1) = \frac{1}{2\pi}\int_0^{2\pi}\frac{R_\omega(\theta_1)}{R_\omega^e(\theta_1)}dK\Lambda,$$

For the sake of simplicity, we use $|C|^2 \approx \frac{R_1}{1 - R_1}$ for both R_ω and R_ω^e, with R_1 the reflectance of a *thick* slab of index n_2 in medium n_1 :

$$R_1 = R_{12} + \frac{R_{12}(1 - R_{12})^2}{1 - R_{12}^2}.$$

Here $R_{12} = \frac{(n_1 - n_2)^2}{(n_1 + n_2)^2}$ is the reflectance at normal incidence between media 1 and 2. As a result, $w(\theta_1)$ is independent of thicknesses d_1 and d_2. We further observe that $w(\theta_1)$ is roughly invariant to N for sufficiently large N. We show the reference correction term $w(\theta_1)$ for discrete values the incident angle and three refractive index values for n_2 (we keep $n_1 = 1$ constant) in Figure 13.

We have empirically found that $w(\theta_1)$ is well approximated using Schlick's formula [Sch94] (solid curves in Figure 13) :

$$\tilde{w}(\theta_1) = \tilde{w}_0 + (1 - \tilde{w}_0)(1 - \cos\theta_1)^5 \approx w(\theta_1),$$

where $\tilde{w}_0 = 0.735R_{12} + 0.532$ is obtained by a linear regression of $w(0)$ for several values of R_{12} (i.e., different (n_1, n_2) pairs).

Appendix C: Absorption term

The integration of the filter F_α over difference angles θ_d yields :

$$\int_0^{\frac{\pi}{2}} F_\alpha(\theta_i, \theta_d)d\theta_d =$$

$$\frac{G_1^2(\theta_i)}{\cos\theta_i}\int_0^{\frac{\pi}{2}}\int_{-\psi_{d_{max}}}^{\psi_{d_{max}}}\tilde{D}(\theta_m)\cos\theta_d\sin\theta_d d\theta_d d\psi_d,$$

where the double integral is equivalent to $\int_\Omega D(\theta_m)\cos\theta_m d\omega_m$. Since $G_1(\theta_i) = \cos\theta_i / \int_\Omega D(\theta_m)\cos\theta_m d\omega_m$ by definition, we get :

$$\int_0^{\frac{\pi}{2}} F_\alpha(\theta_i, \theta_d)d\theta_d = G_1(\theta_i).$$

Appendix D: General Pochi Yeh Equations

We consider a Bragg mirror of refractive indices n_1 and n_2, embedded in a host medium of index n_h.

When $n_h = n_1$, Yeh's formulas (Equations 2 and 9) directly give the reflectance R_ω. Alternatively, we may compute reflectance as $R_\omega = |r_N|^2$, with r_N the reflection coefficient $r_N = \frac{b_0}{a_0}$ where a_0 and b_0 are the incident and the reflected field amplitudes. They are computed using Equation 1, which we rewrite more explicitly following Yeh [Yeh88] :

$$\begin{pmatrix} a_0 \\ b_0 \end{pmatrix} = \begin{pmatrix} \mathcal{V}(A) & \mathcal{U}(B) \\ \mathcal{U}(C) & \mathcal{V}(D) \end{pmatrix}\begin{pmatrix} a_n \\ 0 \end{pmatrix}$$

where we use the following operators :

$$\mathcal{U}(X) = XU_{N-1} \quad\text{and}\quad \mathcal{V}(X) = \mathcal{U}(X) - U_{N-2} = XU_{N-1} - U_{N-2},$$

with $U_N = \frac{\sin((N+1)K\Lambda)}{\sin(K\Lambda)}$ and $X \in \{A, B, C, D\}$.

When $n_h \neq n_1$, Equation 1 is modified by adding an infinitesimal layer of index n_h on top of the Bragg mirror :

$$\begin{pmatrix} a_0 \\ b_0 \end{pmatrix} = \begin{pmatrix} 1 & r_{h1} \\ r_{h1} & 1 \end{pmatrix}\begin{pmatrix} \mathcal{V}(A) & \mathcal{U}(B) \\ \mathcal{U}(C) & \mathcal{V}(D) \end{pmatrix}\begin{pmatrix} a_n \\ 0 \end{pmatrix},$$

with r_{h1} the reflection coefficient between n_h and n_1, computed using Fresnel equations. This yields :

$$\begin{pmatrix} a_0 \\ b_0 \end{pmatrix} = \begin{pmatrix} \mathcal{V}(A) + r_{h1}C & \mathcal{U}(B) + r_{h1}\mathcal{V}(D) \\ \mathcal{U}(C) + r_{h1}\mathcal{V}(A) & \mathcal{V}(D) + r_{h1}\mathcal{U}(B) \end{pmatrix}\begin{pmatrix} a_n \\ 0 \end{pmatrix}.$$

The reflection coeficient is now computed as :

$$r_{hN} = \frac{\mathcal{U}(C) + r_{h1}\mathcal{V}(A)}{\mathcal{V}(A) + r_{h1}\mathcal{U}(C)} = \frac{\left(\frac{\mathcal{U}(C)}{\mathcal{V}(A)} + r_{h1}\right)}{\left(1 + r_{h1}\frac{\mathcal{U}(C)}{\mathcal{V}(A)}\right)} = \frac{r_N + r_{h1}}{1 + r_{h1}r_N},$$

with the corresponding reflectance given by $R_\lambda = |r_{hN}|^2$.